Monthly Notices of the ROYAL ASTRONOMICAL SOCIETY

MNRAS **513,** 405–419 (2022) https://doi.org/10.1093/mnras/stac896
Advance Access publication 2022 April 5

Systematic exploration of heavy element nucleosynthesis in protomagnetar outflows

Nick Ekanger [1★] Mukul Bhattacharya [1,2] and Shunsaku Horiuchi [1,3]

[1] *Center for Neutrino Physics, Department of Physics, Virginia Tech, Blacksburg, VA 24061, USA*
[2] *Department of Physics, Department of Astronomy and Astrophysics, Pennsylvania State University, University Park, PA 16802, USA*
[3] *Kavli IPMU (WPI), UTIAS, The University of Tokyo, Kashiwa, Chiba 277-8583, Japan*

Accepted 2022 March 28. Received 2022 March 23; in original form 2022 January 13

ABSTRACT

We study the nucleosynthesis products in neutrino-driven winds from rapidly rotating, highly magnetized and misaligned protomagnetars using the nuclear reaction network `SkyNet`. We adopt a semi-analytic parametrized model for the protomagnetar and systematically study the capabilities of its neutrino-driven wind for synthesizing nuclei and eventually producing ultra-high energy cosmic rays (UHECRs). We find that for neutron-rich outflows ($Y_e < 0.5$), synthesis of heavy elements ($\overline{A} \sim 20 - 65$) is possible during the first ~ 10 s of the outflow, but these nuclei are subjected to composition-altering photodisintegration during the epoch of particle acceleration at the dissipation radii. However, after the first ~ 10 s of the outflow, nucleosynthesis reaches lighter elements ($\overline{A} \sim 10 - 50$) that are not subjected to subsequent photodisintegration. For proton-rich ($Y_e \geq 0.5$) outflows, synthesis is more limited ($\overline{A} \sim 4 - 15$). These suggest that while protomagnetars typically do not synthesize nuclei heavier than second *r*-process peak elements, they are intriguing sources of intermediate/heavy mass UHECRs. For all configurations, the most rapidly rotating protomagnetars are more conducive for nucleosynthesis with a weaker dependence on the magnetic field strength.

Key words: nuclear reactions, nucleosynthesis, abundances – methods: numerical – stars: magnetars – stars: magnetic field – stars: rotation – stars: winds, outflows.

1 INTRODUCTION

The origin of ultra-high energy cosmic rays (UHECRs) remains an important unresolved question in astrophysics (see Hillas 2005; Kotera & Olinto 2011; Alves Batista et al. 2019; Anchordoqui 2019 for recent reviews). Broadly speaking, there are three key observational quantities which can be used to elucidate their sources. The first is the UHECR energy spectrum. Air shower observatories like Pierre Auger Observatory (PAO; Aab et al. 2015b), Telescope Array (TA; Abu-Zayyad et al. 2013), and HiRes (Abbasi et al. 2009) have measured a suppression in the UHECR flux at the highest energies, compatible with their interactions with the cosmic background radiation as predicted by Greisen (1966) and Zatsepin & Kuz'min (1966); this is the so-called Greisen–Zatsepin–Kuzmin (GZK) cutoff, providing support of the extragalactic nature of UHECR sources. The second observational measure is the arrival directions of UHECRs. A number of studies have reported anisotropic distributions for UHECRs (see e.g. Abreu et al. 2010; Aab et al. 2014c, 2015a), including a correlation with starburst galaxies (Aab et al. 2018). However, directional studies are subject to not just the acceleration, survival, and propagation from the source models, but also to uncertainties of the nuclear composition of UHECRs and extragalactic magnetic fields. Directional information, such as the large-scale anisotropy and lack of anisotropy from the Galactic Centre (Aab et al. 2017), is compatible with many source classes, e.g. active galactic nuclei (AGNs), starburst winds, gamma-ray bursts (GRBs), and others (e.g. Biermann et al. 2016; Aab et al. 2018; Zhang et al. 2018). Therefore, additional observational features are warranted.

The third observational measure is the nuclear composition of UHECRs. The composition is primarily determined by the distribution of particle shower maxima, $X_{\rm max}$, which is proportional to the logarithm of mass number A, and its second moment. Studies with PAO data suggest a population of UHECRs from nitrogen and silicon groups up to iron groups (Aab et al. 2014a, b; Unger, Farrar & Anchordoqui 2015; Batista et al. 2019), which is in statistical agreement with TA (Telescope Array Collaboration 2015; Abbasi et al. 2018; The Pierre Auger Collaboration 2019). However, this method is not precise enough to confirm the composition of individual cosmic rays. Therefore, the precise mass distribution is still under debate. Nevertheless, the pure-proton/proton-helium compositions are generally disfavoured, at least for the highest energies (e.g. The Pierre Auger Collaboration 2019; Jiang, Zhang & Murase 2021; Kuznetsov & Tinyakov 2021).

The composition of UHECRs is particularly informative to their source models. Various types of AGNs, GRBs, and core-collapse supernovae (CCSNe) have been proposed as potential UHECR sites and have already been studied in detail. AGNs, for example, are not expected to produce a heavy-dominated composition (Lemoine & Waxman 2009; Metzger, Giannios & Horiuchi 2011b; Horiuchi et al. 2012) (although the low-luminosity AGN models of Rodrigues et al. 2021 seem to support the notion of heavy element dominated

★ E-mail: enick1@vt.edu

composition at ultra-high energies, based on the galactic cosmic ray composition). On the other hand, CCSNe and related phenomena are more conducive to generating higher fractions of heavy nuclei.

In this paper, we study rapidly rotating and highly magnetized protoneutron stars (PNSs; also known as 'millisecond (ms) protomagnetars') that are formed upon the core collapse of massive stars (Duncan & Thompson 1992; Usov 1992). These newly born magnetars have been discussed as sources of long-duration GRBs (Wheeler et al. 2000; Thompson, Chang & Quataert 2004; Metzger et al. 2011a), that can accelerate protons (Arons 2003; Kotera 2011) and heavier particles (Metzger et al. 2011b; Horiuchi et al. 2012; Zhang et al. 2018) to ultra-high energies, making these PNS central engines promising sources of heavier UHECRs. Magnetar theory more generally has also been linked more recently to GRB observations (e.g. Margutti et al. 2013, 2014) and used to constrain magnetic field strength and spin period using X-ray afterglow plateau data (e.g. Zhang & Mészáros 2001; Lü & Zhang 2014).

Here, we consider relativistically expanding winds launched by PNS and study their composition as a function of the source magnetic field strength and spin period. Not all configurations of magnetic field and spin period may lead to successful GRBs. Alternatively, winds embedded inside of their progenitor/supernova are not freely expanding, and in the extreme case, outflows can be choked (e.g. Metzger et al. 2011a). However, the parameter space where this happens is highly uncertain and also dependent on the progenitor model, and we defer this to a future investigation. Note that our focus also contrasts with more typical pulsars with lower field strengths, which represent a sufficiently different scenario, where nucleosynthesis and particle acceleration are coupled and the results may be significantly different from those found in this work (see Fang, Kotera & Olinto 2012).

A number of papers have analytically studied the composition of CCSNe outflows more broadly (e.g. Qian & Woosley 1996; Hoffman, Woosley & Qian 1997; Metzger et al. 2011b) but there is a benefit of using numerical treatments that allow the study of these systems in extraordinary detail. With large networks of nuclides and reactions, one can study the time evolution of abundance patterns of thousands of nuclei. Nuclear reaction networks like `SkyNet` (Lippuner & Roberts 2017), `WinNet` (Winteler 2014), and `PRISM` (Mumpower et al. 2017) have been applied to a number of astrophysical scenarios including CCSNe outflows (e.g. Roberts, Woosley & Hoffman 2010; Arcones & Montes 2011; Halevi & Mösta 2018; M'osta et al. 2018; Grimmett et al. 2020; Reichert et al. 2021), NS–NS and neutron star-black hole (NS–BH) mergers (e.g. Roberts et al. 2016; Lippuner & Roberts 2017; Côté et al. 2018; Chen et al. 2021). In particular, although NS–NS mergers are considered the primary source (e.g. Abbott et al. 2017; Yong et al. 2021), CCSNe are an additional proposed source for *r*-process elements in the universe. These sources would have to agree with the solar abundance patterns and those of ultra-metal-poor (UMP) stars (Arnould, Goriely & Takahashi 2007; Sneden, Cowan & Gallino 2008; Yong et al. 2021). NS–NS merger events may also be inefficient accelerators of heavy nuclei, making alternative transient phenomena worthy of study (Kyutoku & Ioka 2016). There is, in fact, some observational evidence for the association of *r*-process elements and hypernovae (Skuladottir et al. 2021; Yong et al. 2021).

For the scope of this study, we use the nuclear reaction network `SkyNet` to understand the composition of protomagnetar outflows as a function of their physical parameters. We show that heavy nuclei ($A > 82$, first r-process peak) are synthesized in lesser quantities compared to previous analytic studies (e.g. Metzger et al. 2011b; Bhattacharya, Horiuchi & Murase 2021), but the results support an intermediate-mass composition ($\overline{A} \sim 10 - 50$) which can eventually become UHECRs. The paper is structure as follows. In Section 2, we describe our physical model, its tunable model parameters, and the nuclear network used. In Section 3, we discuss the nucleosynthesis results as a function of the model parameters. In Section 3.2, we discuss the general trends in our results and extend this discussion to a broader context. Finally, we conclude in Section 3.2.

2 PROTOMAGNETAR MODEL AND NUCLEAR NETWORK

2.1 Protomagnetar outflow properties

The model for the protomagnetar outflows comes primarily from the neutrino-driven winds prescription of Qian & Woosley (1996; hereafter QW96), the protomagnetar-GRB model of Metzger et al. (2011a), and updates from Metzger et al. (2011b). Metzger et al. (2011b) used the analytical models of primarily QW96, Hoffman et al. (1997), and Metzger et al. (2011a) to estimate heavy element nucleosynthesis in the context of UHECRs. We build on these models to numerically study the outflow composition, which is useful to confirm the key results of analytical studies and reveal more detailed information on the composition of magnetar outflows.

We first describe our modelling of the neutrino-driven outflows launched from rapidly rotating protomagnetars. The important quantities of interest are the wind mass-loss rate, entropy per baryon, and outflow expansion time-scale, given by (see Appendix A, Table A1 for a description of all symbols used in this work)

$$\dot{M} = 4\pi r^2 \rho v f_{\rm open} f_{\rm cent}, \tag{1}$$

$$S = \frac{4\pi^2 m_N k_B}{45} \frac{T^3}{\rho} \frac{1}{(\hbar c)^3}, \tag{2}$$

$$\tau_{\rm exp} = \frac{r}{v}\Big|_{T_{\rm rec}}, \tag{3}$$

where the outflow quantities $\dot{M}$, r, ρ, v, S, T, $\tau_{\rm exp}$, and $T_{\rm rec}$, are the mass-loss rate, radial coordinate of the outflow, mass density at the radial coordinate, velocity at radial coordinate, entropy, temperature, expansion time-scale, and recombination temperature, respectively (see QW96). We modify the spherical mass-loss rate with $f_{\rm open}$, the fraction of the PNS surface that is threaded by open magnetic field lines, and with $f_{\rm cent}$, the factor that enhances mass-loss rate due to a magnetocentrifugal slinging effect. Here, $f_{\rm open}$ is approximated as $(1 + \sin^2\chi)^{1/2} R_{\rm NS}/2R_Y$ where, in this work, obliquity angle $\chi = \pi/2$, $R_{\rm NS}$ is the NS radius, and R_Y is the last radius where the magnetic field lines are closed (Metzger et al. 2011a) and $f_{\rm cent} = f_{\rm cent,\,max}(1 - \exp[-R_A/R_s]) + \exp[-R_A/R_s]$, where $R_A = R_L \min(\sigma_0^{1/3}, 1)$ is the Alfven radius, $R_L = c/\Omega$ is the light cylinder radius, $\Omega = 2\pi/P$ is the PNS angular velocity, P is the spin period, and $R_s = (GM/\Omega^2)^{1/3}$ is the sonic radius (Lamers & Cassinelli 1999; Metzger, Thompson & Quataert 2007). $f_{\rm cent,\,max} = \exp[(P_{\rm cent}/P)^{1.5}]$, where $P_{\rm cent} = (2.1\,{\rm ms}) \sin\alpha\, (R_{\rm NS}/10\,{\rm km})^{3/2} (M_{\rm NS}/1.4\,{\rm M}_\odot)^{1/2}$, $\alpha = \max(\theta_{\rm open}/2, \chi)$, and $\theta_{\rm open}$ is the opening angle of the polar cap ($M_{\rm NS}$ is the NS baryonic mass; Metzger, Thompson & Quataert 2008).

The $\dot{M}$ correction terms, $f_{\rm open}$ and $f_{\rm cent}$, both evolve while the PNS cools down as R_Y, R_A, and R_s are all time-dependent quantities. These corrections are valid only within the light cylinder. This step is relevant for our purposes as nucleosynthesis concludes around the light cylinder radius. In reality, the outflow may be collimated due to its interaction with the surrounding cocoon as the jet propagates through the stellar material, but this typically occurs on much larger radii as compared to nucleosynthesis.

Combining equations (1) and (3) gives

$$\rho = \frac{\tau_{\rm exp}\dot{M}}{4\pi r^3}(f_{\rm open} f_{\rm cent})^{-1}, \tag{4}$$

$$T = \left(\frac{45\rho S}{4\pi^2 m_N k_B}\right)^{1/3} \hbar c, \tag{5}$$

where m_N is the nucleon mass. Different corrections to the mass-loss rate and outflow geometry can result in different density profiles. For instance, Metzger et al. (2011b) uses an areal function of the flux tube correction that leads to $\rho \propto r^{-3}$ inside the light cylinder in contrast to $\rho \propto r^{-2}$ for larger radial distances $r \gtrsim R_{\rm Y}$. This transition in the mass density profile at the light cylinder radius can also influence the nucleosynthesis yields (see Vlasov et al. 2017, for detailed discussions). However, in this work, we adopt the areal function of the dipolar flux tube from Metzger et al. (2011a) for consistency. We estimate the protomagnetar wind mass-loss rate, outflow entropy, and outflow expansion time-scale (equations 1, 2, and 3) with equations (58a), (48a), and (61) from QW96 and updated in Metzger et al. (2011a). We also include a ~ 20 per cent general relativistic enhancement to the entropy

$$\dot{M} = \left(5\times10^{-5}\,{\rm M_\odot\ s^{-1}}\right) f_{\rm open} f_{\rm cent} \times C_{\rm es}^{5/3} L_{\nu,52}^{5/3} \epsilon_{\nu,10}^{10/3} R_{10}^{5/3} M_{1.4}^{-2}, \tag{6}$$

$$S = \left(88.5\,{\rm k_B\ nuc^{-1}}\right)\ C_{\rm es}^{-1/6} L_{\nu,52}^{-1/6} \epsilon_{\nu,10}^{-1/3} R_{10}^{-2/3} M_{1.4}, \tag{7}$$

$$\tau_{\rm exp} = (68.4\ {\rm ms})\ C_{\rm es}^{-1} L_{\nu,52}^{-1} \epsilon_{\nu,10}^{-2} R_{10} M_{1.4} f_{\rm open}, \tag{8}$$

where $C_{\rm es}$ is a heating correction from neutrino-electron scattering (see QW96 equations 50 and 51a), $L_{\nu,52} = L_\nu/10^{52}\,{\rm erg\,s^{-1}}$, $\epsilon_{\nu,10} = \epsilon_\nu/10\,{\rm MeV}$, $R_{10} = R_{\rm NS}/10\,{\rm km}$, and $M_{1.4} = M_{\rm NS}/1.4\,{\rm M_\odot}$.

We adopt the dynamical neutrino quantities for a $1.4\,{\rm M_\odot}$ PNS given in Pons et al. (1999) and assume that the electron and anti-electron neutrinos have similar L_ν and ϵ_ν evolution with time. Given that Pons et al. (1999) does not account for a rotating progenitor, stretching the neutrino quantities accounts for the increased time-scale for NS cooling due to rotation. We follow Metzger et al. (2011a) for this procedure: we take $L_\nu \rightarrow L_\nu|_{\Omega=0}\ \eta_s^{-1}, t \rightarrow t|_{\Omega=0}\ \eta_s, \epsilon_\nu \rightarrow \epsilon_\nu|_{\Omega=0}\ \eta_s^{-1/4}$ where $\Omega = 0$ represents the non-rotating cases and η_s is the stretch factor fixed to 3. Rapidly rotating NSs with misaligned magnetic fields and rotation axes also experience a suppression in entropy. To account for the reduced neutrino heating as a result of centrifugal acceleration due to rapid rotation, we apply an exponential suppression factor: $S_{\rm rot} = S \times \exp[-P_{\rm cent}/P]$.

2.2 Post-launch evolution

The distance of the jet-head from the central engine (where, specifically, the jet refers to the collimated, relativistic outflow) is determined from[1] (Drenkhahn 2002)

$$\beta_j \Gamma_j = \begin{cases} \sigma_0 (r/R_{\rm mag})^{1/3}, & r < R_{\rm mag} \\ \sigma_0, & r > R_{\rm mag}, \end{cases} \tag{9}$$

where

$$R_{\rm mag} = (5\times10^{12}\ {\rm cm}) \left(\frac{\sigma_0}{10^2}\right)^2 \left(\frac{\rm P}{\rm ms}\right) \left(\frac{\epsilon}{0.01}\right)^{-1}, \tag{10}$$

[1]Note the original expression is in the relativistic limit; here, we multiply by an additional β_j factor, which allows us to model the outflow through the sub-relativistic regime as well.

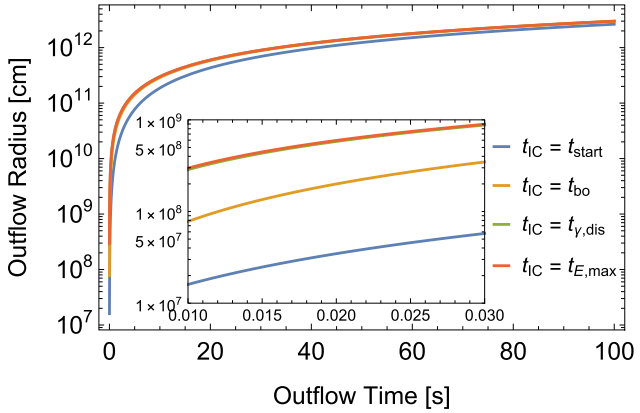

Figure 1. Outflow radius over outflow time for $B_{\rm dip} = 5\times10^{14}$ G, $P_0 = 1.5$ ms for four outflow launch times of interest (initial condition times $t_{\rm IC}$, see Section 2.3 for description). Inset figure shows the outflow radius at the earliest outflow times. The time when the outflow velocity approaches the speed of light depends on the initial conditions, but generally takes only a few seconds. The starting point of each outflow at $t = 0$ s is from the PNS surface at $R_{\rm NS} \sim 12-30$ km, depending on the IC time when each outflow begins.

is the magnetic saturation radius. Here, σ_0 is the magnetization as described below, and ϵ is a parameter used to describe the reconnection speed (here, ϵ is assumed to be 0.01). Rearranging further gives ${\rm d}r/{\rm d}t = c(\alpha/\sqrt{1+\alpha^2})$, where $\alpha = \sigma_0(r/R_{\rm mag})^{1/3}$. The outflow velocity quickly becomes relativistic, with a weak dependence on the initial outflow conditions σ_0 and $R_{\rm mag}$ (see Fig. 1). At later launch times, the magnetar outflows become ultrarelativistic more quickly than at early launch times, but in general, ${\rm d}r/{\rm d}t$ approaches c within $\sim 1-5$ s. The initial magnetization of the outflow at launch is defined as

$$\sigma_0 = \frac{\phi^2\Omega^2}{\dot{M}c^3}, \tag{11}$$

where $\phi = (f_{\rm open}/4\pi) B_{\rm dip} R_{\rm NS}^2$ is the magnetic flux threading the open magnetosphere and $B_{\rm dip}$ is the dipolar magnetic field strength.

If the central engine and outflow are active for long enough, the jet eventually breaks out of the progenitor. The jet breakout time is then given by (Bhattacharya et al. 2021)

$$t_{\rm bo} = (4.2\ {\rm s}) \left(\frac{\rm B_{dip}}{3\times10^{15}\ {\rm G}}\right)^{-1/3} \left(\frac{\rm P_0}{3\ {\rm ms}}\right). \tag{12}$$

This is based on the breakout-time analytical fit given by Bromberg, Granot & Piran (2015) and assumes a magnetized, Poynting-flux dominated jet with opening angle $\theta_j = 7^\circ$ that can be collimated by the interactions with the stellar material. Equation (12) is obtained assuming a $15\,{\rm M_\odot}$ and $4\,{\rm R_\odot}$ Wolf–Rayet star with stellar density profile $\rho \propto r^{-2.5}$, and is applicable for $B_{\rm dip}$ between $[3\times10^{14}, 3\times10^{16}]$ G and P_0 between $[1.0, 5.0]$ ms, as considered in Bhattacharya et al. (2021), which includes the parameter range considered in this work.

At large radial distances after breakout ($r \sim 10^{13} - 10^{16}$ cm), the jet dissipates its energy either through internal shocks or magnetic reconnection. During this dissipation phase, the jet powers high-energy gamma-ray emission (the GRB). It is also during this dissipation that the nuclei synthesized in the neutrino-driven outflows are accelerated to ultra-high energies (Metzger et al. 2011b). We use the magnetic reconnection model of Drenkhahn & Spruit (2002), where dissipation occurs from small outflow radius up to the saturation

radius, $R_{\rm mag}$ (equation 10). We consider first-order Fermi acceleration with a characteristic time-scale similar to the Larmor gyration time-scale. For nuclei to be accelerated, this acceleration time-scale must be smaller than the time-scales for jet expansion and synchrotron cooling; this condition determines the maximum UHECR energy. Soon after core collapse, synchrotron cooling is more restrictive but in the regime that concerns us, the expansion time-scale limits the maximum energy (see Bhattacharya et al. 2021, fig. 9, for further details).

For heavy nuclei to survive and escape the GRB, they must first endure some critical number of photodisintegration interactions. This number of interactions, or photodisintegration optical depth $\tau_{\gamma-N}$, is estimated assuming a Band prompt emission spectrum for the surrounding photon field (Bhattacharya et al. 2021), and is given as

$$\tau_{\gamma-N} \approx \frac{\dot{E}_{\rm iso}\varepsilon_{\rm rad} C \sigma_{\rm GDR}(\Delta\epsilon_{\rm GDR}/\bar{\epsilon}_{\rm GDR})}{4\pi\epsilon_p r c \Gamma_j^2}, \tag{13}$$

where $\dot{E}_{\rm iso}$ is the isotropic jet luminosity, $\varepsilon_{\rm rad} \sim 0.1-1$ is the radiative efficiency of the jet, and $C \sim 0.2$ is the fraction of gamma-ray photons released below the peak energy $\epsilon_p \sim 0.1-1$ MeV of the Band spectrum (Metzger et al. 2011b). Since giant dipole resonances dominate the energy-loss processes, the relevant resonance width $\Delta\epsilon_{\rm GDR}/\bar{\epsilon}_{\rm GDR} \sim 0.4\,(A/56)^{0.21}$ and cross-section $\sigma_{\rm GDR} \sim 8 \times 10^{-26}\,(A/56)\,{\rm cm}^2$ are used (see Khan et al. 2005; Murase et al. 2008). We conservatively use this collisional optical depth since the inelasticity of collisions is typically $\lesssim 10$ per cent. Including a treatment for inelastic collisions generally broadens the time by about 10 s between our photodisintegration and max acceleration IC times (see Section 2.3) thereby allowing more heavy nuclei to be synthesized and accelerated to UHECR energies (see Bhattacharya et al. 2021). Also, our expression assumes a pure iron composition, and thus is a conservative estimate, since one photodisintegration event does not fully destroy the heavy nuclei. In fact, since the nuclei scattering inelasticity factor is typically $\lesssim 10$ per cent, we can expect that a photodisintegration optical depth of a few will still maintain a heavy ultra-high energy cosmic ray population.

2.3 Model parameters

We next describe the parameter choices for our systematic study of nucleosynthesis in protomagnetar outflows. The nucleosynthesis depends on the properties of the outflow, which in turn depend on the protomagnetar and its time evolution.

Our semi-analytic protomagnetar model primarily depends on the surface dipole field strength $B_{\rm dip}$ and initial spin period P_0 of the protomagnetar. We adopt six $B_{\rm dip}$ values between $[5 \times 10^{14}, 1 \times 10^{16}]$ G and five P_0 values between [1.5,3.5] ms. We must also specify the electron fraction $Y_e = n_p/(n_n + n_p)$ of the outflow, where $n_p(n_n)$ are proton(neutron) densities. There is currently significant uncertainty in the value of Y_e and its evolution over time, and our protomagnetar model does not self-consistently compute them. Instead, we adopt four fixed electron fraction values around and including 0.5, and assume them to not depend on $B_{\rm dip}$, P_0 or vary over time. In our study, we do not account for the νp-process (Fröhlich et al. 2006; Arcones & Montes 2011) that would change the electron fraction and increase the neutron-to-seed ratio.

Once these parameters are set, the protomagnetar evolves over time according to our semi-analytic model as described in the previous sections. We describe this evolution using the notation of 'Initial Condition' (IC) time: IC times are characteristic post-core-collapse times that represent physical stages in the protomagnetar evolution. Early IC times define the head of the jet, while later IC times define later parts of the jet. In this way, IC time can also be thought of as different locations within the magnetized jet.

We explore nucleosynthesis at four specific IC times (consequently, locations in the jet) corresponding to four physical epochs, as described below (also see Bhattacharya et al. 2021). In reality, the system ejects material continuously, not just at four epochs, and the overall jet composition is the superposition of this continuous outflow. The discretization of the continuous outflow into our four IC times serves to estimate the composition at four physically different epoch/locations. Although, in principle, the outflows can last for longer time-scales (up to $\sim 10^3$ s for GRB emission and $\sim 10^4$ s for X-ray plateaus), our final IC time marks the end of the epoch relevant for accelerating UHECRs. Around $t_{\rm E,\,max}$ (details below), the outflows become optically thin to neutrinos (Bhattacharya et al. 2021) and the mass-loss rate begins to fall off significantly.

To summarize, we consider the following values:

- $B_{\rm dip}$ (G): 5×10^{14}, 7.5×10^{14}, 1×10^{15}, 2.5×10^{15}, 5×10^{15} and 1×10^{16}
- P_0 (ms): 1.5, 2, 2.5, 3, 3.5
- Y_e: 0.45, 0.475, 0.5, 0.55
- IC time: we consider the following four times

(i) Start ($t_{\rm start}$): ~ 0.5 s. This is when the outflow starts, assumed to be the same for all protomagnetar configurations.

(ii) Jet breakout ($t_{\rm bo}$): The time when the bipolar outflow breaks out of the progenitor envelope. Depends on $B_{\rm dip}$ and P_0 as well as the progenitor and jet dynamics assumptions. We adopt equation (12). Outflows before this time have not escaped from the star.

(iii) Photodisintegration time ($t_{\gamma,\,\rm dis}$): Even if the outflow contains nuclei they can be destroyed during the outflow evolution. We define the photodisintegration time to be when the majority of synthesized heavy elements survive photodisintegration during particle acceleration at the dissipation radius, i.e. the number of interactions that can destroy nuclei ($\tau_{\gamma-N}$, equation 13) ≈ 1. This depends on $B_{\rm dip}$ and P_0.

(iv) Max acceleration time ($t_{\rm E,\,max}$): The maximum energy reached by accelerated nuclei is determined by the balance of the acceleration time and energy loss times, and generally shows a peak before falling with time. We define the max acceleration time as the final time when heavy nuclei can be accelerated above a maximum energy of 10^{20} eV; after this time, the maximum energy reached is $< 10^{20}$ eV. We assume a pure iron composition for this calculation, and the resulting time depends on $B_{\rm dip}$ and P_0 (see Bhattacharya et al. 2021).

Prior to $t_{\rm bo}$, any nuclei synthesized will not make it out of the star unscathed, and hence, we assume they cannot become UHECRs. However, $t_{\rm start}$ has its uses. Analysing the nucleosynthesis products at a specific time (independent of $B_{\rm dip}$ and P_0, at ~ 0.5 s) provides a benchmark to extract some of the qualitative dependencies of initial magnetar properties to the final results. This specific time is chosen to reduce the effect of numerical artifacts at very early times.

The most significant epoch at which protomagnetar outflows can contribute to the UHECR composition is between the photodisintegration and max acceleration times – where nuclei can be synthesized, avoid photodisintegration, and be accelerated to ultra high energies. We stress, however, our conditions are conservative, and that in reality, some heavy nuclei are expected to survive even between $t_{\rm bo}$ and $t_{\gamma,\,\rm dis}$.

Although our adopted photodisintegration and maximum acceleration times depend on the assumption that the outflow is dominated by a pure iron composition, this is not a strong dependence (see

Bhattacharya et al. 2021) and therefore they can be used as a proxy for the true time. Improving the IC times and resolution in parameter space is left for future study.

There is an inherent uncertainty about the time evolution of Y_e in magnetars' neutrino-driven outflows. The true electron fraction in protomagnetar outflows may vary as the equilibrium Y_e (see QW96, equation 77), but will still depend implicitly on the neutrino luminosities, the neutrino mean energies, and the dynamical evolution of the PNS. Furthermore, it is impacted by the effects of neutrino oscillations, which undergo potentially time-varying collective oscillations. In light of these uncertainties, we test nucleosynthesis for fixed Y_e as an independent model parameter. Since we consider four IC times independently of our choices of Y_e, we can use different combinations to make qualitative statements for any assumed time evolution of Y_e (within the range considered here).

2.4 Nuclear reaction network

To calculate nucleosynthesis in protomagnetar outflows, we use the nuclear reaction network `SkyNet` (Lippuner & Roberts 2017). `SkyNet` uses a modified Helmholtz equation of state (Timmes & Douglas Swesty 2000) that supports initial densities up to $10^{11}\,\mathrm{g\,cm^{-3}}$. All models tested in this work begin with densities lower than this limit. Most configurations of $B_{\rm dip}$ and P_0 begin their thermodynamic trajectories with temperatures above the 7 GK threshold for nuclear statistical equilibrium (NSE); after outflow temperatures decrease beyond this threshold, full network evolution kicks in.

We use 93 271 forward reaction rates from JINA REACLIB (Cybert et al. 2010) and inverse reactions are calculated with detailed balance to ensure consistency with NSE. Masses and partition functions for nuclear species are used from WebNucleo XML included with REACLIB. Finally, 7836 nuclear species are evolved up to $Z = 112$, $A = 337$.

To produce the thermodynamic trajectories (density, temperature, and electron fraction with time) necessary for `SkyNet`, we make a few simplifying assumptions. The magnetization, entropy, mass-loss rate, and expansion time-scale (σ_0, S, $\dot{M}$, $\tau_{\rm exp}$) all evolve with time. However, since we want to probe the outflow composition at four epochs, we evaluate these quantities at the four IC times and keep them constant in Outflow time. Hence, we call them 'ICs'; they determine the outflow properties at a given IC time, but remain constant in Outflow time. This is primarily justified because nucleosynthesis concludes after ~ 10 ms in general (see Fig. 2) and these quantities are approximately constant in that time. We account for the evolution of the thermodynamic trajectories due to the expansion of the outflow into the progenitor by numerically solving the $\mathrm{d}r/\mathrm{d}t$ equation for outflow radius over time. In this way, the initial densities and temperatures are set by the ICs and then evolve according to the radial coordinate time evolution. For all trajectories, we evolve the network until 100 s in Outflow time. Appendix B discusses how these ICs depend on the protomagnetar parameters.

3 RESULTS

3.1 Abundance patterns

In Fig. 3, we show the distributions of abundances Y_i for species i, where $\sum_i Y_i$ is normalized to 1. We show for a fixed $Y_e = 0.45$ at four different IC times (left-hand panel) and at max acceleration time for four Y_e (right-hand panel) for a magnetar with $B_{\rm dip} = 5 \times 10^{14}$ G and $P_0 = 1.5$ ms. In all scenarios, significant amounts of free nucleons

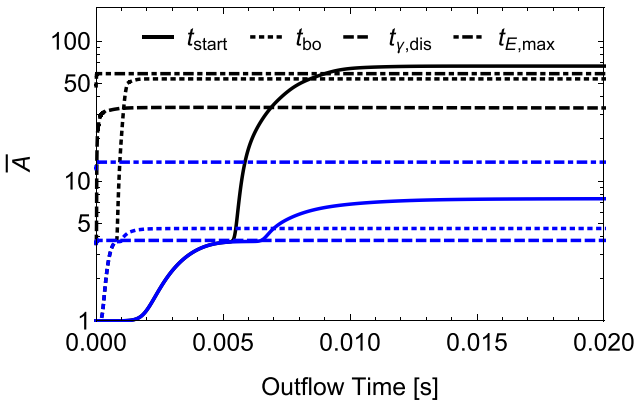

Figure 2. Mean mass number of the outflow as a function of outflow time for $B_{\rm dip} = 5 \times 10^{14}$ G, $P_0 = 1.5$ ms model. Evolution is shown for two extremal electron fractions (black lines for $Y_e = 0.45$ and blue lines for $Y_e = 0.55$) and four IC times (as labelled). $\overline{A}$ first saturates to helium-4 before heavier elements are synthesized. For all launch times, nucleosynthesis concludes by ~ 10 ms post launch.

and helium are formed, but in proton-rich conditions and at late times, they become more significant compared to heavy elements. At early IC times after core collapse, the abundance pattern peaks at nickel-62 ($t_{\rm start}$) and above the first *r*-process peak at strontium-88 ($t_{\rm start}$ and $t_{\rm bo}$). At late IC times ($t_{\gamma,\,\rm dis}$ and $t_{\rm E,\,max}$), heavier elements are formed, but in smaller quantities, including nuclei near the second *r*-process peak ($A \sim 130$). This trend continues as time progresses.

As a function of Y_e, more neutron-rich conditions favour heavy nucleosynthesis with larger relative abundances, while with proton-rich conditions, the opposite is true. Generally, across all other configurations of $B_{\rm dip}$ and P_0, these trends hold true. There is an important exception in this particular configuration: at the max acceleration time, $t_{\rm E,\,max}$, the abundance pattern resembles more closely the pattern at $t_{\rm start}$ (see Section 3.2 for more details). Although the trends in IC time are generally monotonic among other configurations, the ICs at this time result in an overall higher mean mass number (see Appendix B for the ICs of all configurations).

The majority of configurations do not synthesize third *r*-process peak elements ($A \sim 196$) because the outflow entropies are much too low, their expansion time-scales too long, and their neutron-to-seed ratios are quite small (see Hoffman et al. 1997; Nagataki & Kohri 2001; Thompson, Burrows & Meyer 2001). In other words, the figure of merit parameter for these outflows is always below the critical value required for the synthesis of third *r*-process peak elements (Hoffman et al. 1997). However, for configurations with $Y_e = 0.5$ at $t_{\gamma,\,\rm dis}$ and $t_{\rm E,\,max}$, third *r*-process peak nuclei are synthesized, albeit in very small abundances by mass. For some regions of parameter space in entropy and expansion time-scale, a particular process occurs. Below NSE, there is a persistent disequilibrium between free nucleons and helium nuclei. Even a small abundance of free nuclei can then become seeds for the available free nucleons. These are captured readily by the seeds and what is left is dominated by mass in alpha particles, but with almost negligible abundances of very heavy nuclei. These include *r*-process elements, but do not match with solar abundances. This process is sensitive not just to the entropy and expansion time-scale, but also to electron fraction. It can also occur for outflows that are only slightly neutron- or proton-rich, but becomes less effective when Y_e moves farther away from 0.5 (see Meyer 2002 for details on the process and Fujibayashi, Yoshida & Sekiguchi 2016 for another example).

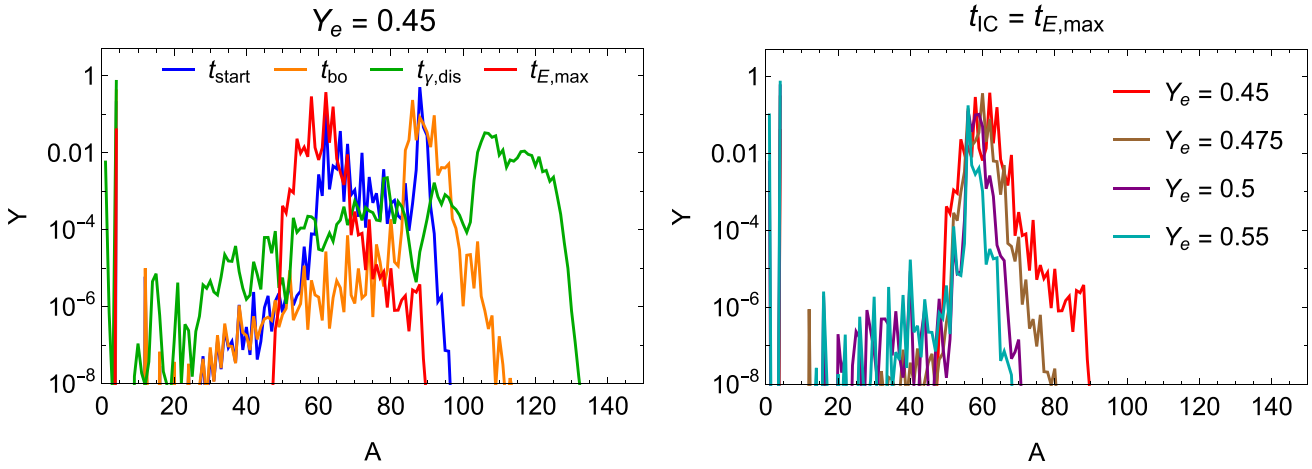

Figure 3. Left-hand panel: Abundance pattern for an electron fraction of $Y_e = 0.45$ is shown for the $B_{dip} = 5 \times 10^{14}$ G, $P_0 = 1.5$ ms model at four IC times. Right-hand panel: Abundance pattern at the final IC time, when max nuclei acceleration occurs, is shown for four Y_e values. In both panels, if isotopes have the same mass number, their abundances are added.

Our results are broadly consistent with studies of nucleosynthesis under similar conditions. For example, Vlasov et al. (2017) explored nucleosynthesis with SkyNet under a comparable protomagnetar parameter space. They adopted a force-free derived field structure in contrast to our simple analytic model, but found abundance patterns similar to those shown in Fig. 3. A notable feature common to both is the negligible abundance of $Z = 41$ (present in some, not all configurations of the model parameters explored here). For the model with $B_{dip} = 1 \times 10^{16}$ G, $P_0 = 3$ ms, $Y_e = 0.45$, at t_{start}, we carried the calculation out to 10^9 s in Outflow time. Between 100 and 10^9 s, isotopes of niobium with mass numbers $A = 94$, 96, 98, 99, 100, 101, 102, 103, and 105 underwent complete decay. In addition, Surman et al. (2014) and Bliss et al. (2017) study the weak *r*-process under similar astrophysical conditions and comparable entropies and electron fraction. These studies confirm an abundance pattern that peaks around these nickel- and strontium-like nuclei. Bliss et al. (2017) also confirms a negligible abundance of nuclei near $Z = 41$. Finally, other magnetorotational studies (e.g. Winteler 2014; Halevi & Mösta 2018; M'osta et al. 2018) also show successful synthesis of heavy elements, although the magnetic field strengths and electron fractions are generally lower than the corresponding values considered in this work.

3.2 Mean composition trends

To quantify how much nucleosynthesis occurs, we express the results in terms of abundance-weighted mean mass number and mass fraction of nuclei heavier than iron ($A \geq 56$), that is

$$\overline{A} = \sum_i Y_i A_i \Big/ \sum_i Y_i, \tag{14}$$

$$X_h = \sum_{A \geq 56} X_i \Big/ \sum_i X_i, \tag{15}$$

where $X_i = Y_i \times A_i / \sum_i Y_i \times A_i$ is the mass fraction for species i (see Appendix C for a discussion on the analytic estimation of X_h with the parameter space considered here).

In Fig. 4, we show the mass fraction above iron and mean mass number for the same model as in Fig. 3. X_h (per cent) and $\overline{A}$ show the same trends: significant nucleosynthesis in neutron-rich conditions and then a sharp decrease as the outflow becomes more and more

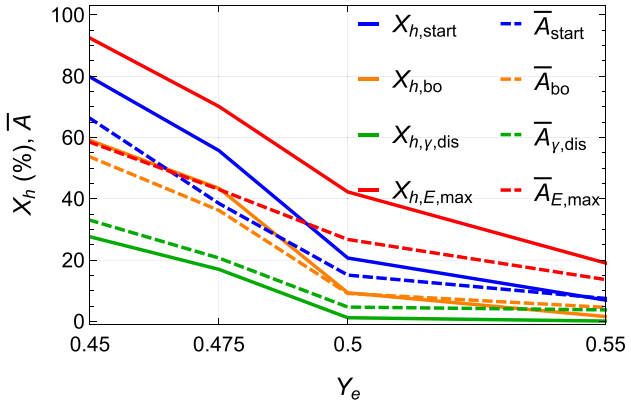

Figure 4. The mass fraction of nuclei heavier than iron (X_h, in per cent, solid lines) and the mean mass number ($\overline{A}$, dashed lines) as functions of electron fraction (see equations 14 and 15). The results are shown for four IC times for the $B_{dip} = 5 \times 10^{14}$ G, $P_0 = 1.5$ ms model.

proton-rich. As IC time increases, synthesis reaches higher mass numbers (see Fig. 3), but in small quantities, resulting in smaller X_h and $\bar{A}$ than at earlier times. The exception to this is at $t_{E,max}$, when $\overline{A}$ is higher than expected, as we saw also in Fig. 3. We have found that this does occur for other configurations with $P_0 = 1.5$ ms, but is especially pronounced for the case of $B_{dip} = 5 \times 10^{14}$ G. In proton-rich conditions, the nucleosynthesis products are increasingly dominated by free nucleons and helium as IC time increases.

Finally, in Fig. 5, we show the results of nucleosynthesis in protomagnetar outflows in terms of mean mass number as a function of the four model parameters: B_{dip}, P_0, Y_e, and IC time. Note that the contours, i.e. the range and scale of $\overline{A}$, are different for each panel. These panels continue to show the same trends as in the previous figures, but also display the effects of the dipolar field and initial spin period on the final abundance of heavy elements.

At early IC times (t_{start} and t_{bo}), a smaller magnetic field is more conducive to nucleosynthesis and this trend generally switches at late IC times ($t_{\gamma,dis}$ and $t_{E,max}$). SkyNet determines these trends from the density and temperature trajectories: generally, at t_{start} and t_{bo}, the densities are higher for the low-B_{dip} configurations and the opposite

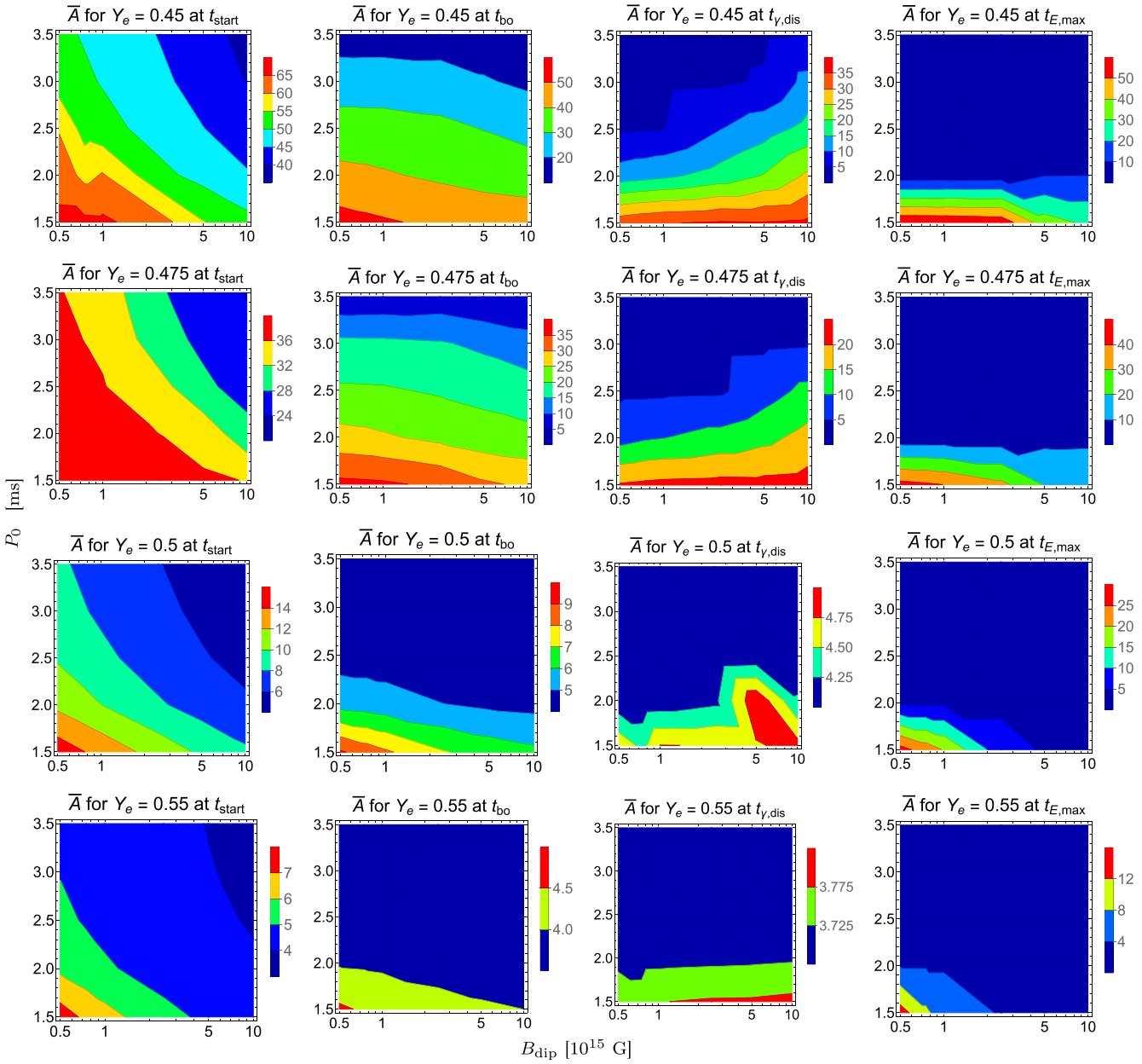

Figure 5. In each panel, we show the mean mass number $\bar{A}$ in the $B_{dip} - P_0$ plane. Top-to-bottom: for electron fraction $Y_e = 0.45, 0.475, 0.5, 0.55$. Left-to-right: for our four chosen IC times: start time, breakout, photodisintegration, and max acceleration time. Note that the colour range in each panel shows a different scale.

is true at $t_{\gamma,\,dis}$ and $t_{E,\,max}$ (see Appendix B). An increased initial density leads to increased neutron-capture reaction rates and, with longer expansion time-scales, there is more time for the free neutrons to capture on to seed nuclei (see Hix & Thielemann 1999; Lippuner & Roberts 2015; Fujibayashi et al. 2016). On the other hand, entropy does not vary much in B_{dip} (see Appendix B, Fig. B1). Since $T \sim S^{1/3}$, outflow entropy does not play a significant role in determining the trend of $\bar{A}$ relative to B_{dip}. The trends we observe then must come from τ_{exp} and $\dot{M}$; in turn, the B_{dip} dependence for these quantities come from f_{open} and f_{cent}. Traditionally, shorter expansion time-scales are required for strong *r*-process to occur, however in our outflow system, a longer expansion time-scale gives rise to larger outflow densities (see equation 4). These larger densities (at moderate initial temperatures) give rise to the aforementioned enhanced neutron-capture rate and higher mean mass numbers. Since τ_{exp} and $\dot{M}$ are greater for low-B_{dip} configurations at early times, this increased density gives higher values of $\bar{A}$. After t_{bo}, centrifugal slinging increases for higher magnetic field strengths (as f_{cent} increases), driving a high-B_{dip} preference for $\dot{M}$. This gives the transition in the magnetic field preference for $\bar{A}$ (and ρ).

Entropy plays a larger role as the rotation rate is changed: since the entropy suppression is directly related to the spin period, we have higher initial temperatures for slower rotators. These higher initial temperatures lead to lower $\bar{A}$ values from increased photodisintegration effects. The final $\bar{A}$ also depends on the outflow density, whose P_0 trends are set by the factor ~ 5 difference in f_{open} as the rotation rate changes structure of the open magnetic field lines. With decreased photodisintegration and enhanced nucleon-capture reaction rates

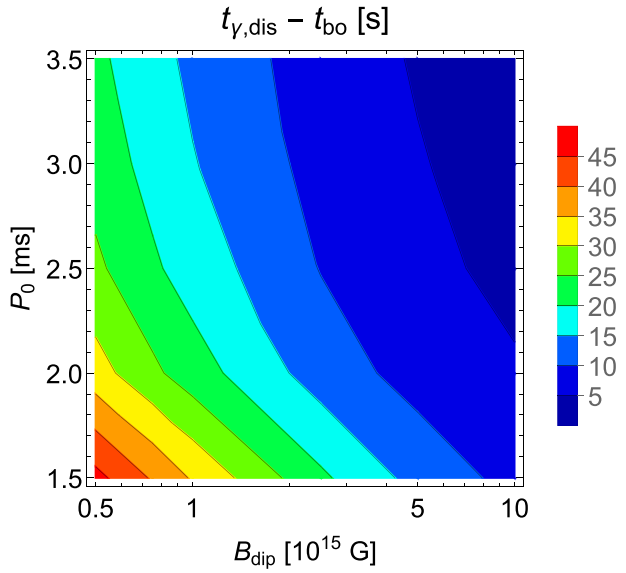

Figure 6. The time elapsed between jet breakout and when photodisintegration is no longer important (see Appendix B, Fig. B2 for the individual time values). In this time window, any nuclei synthesized can be accelerated but the majority will be disintegrated, though some amount may survive as heavy nuclei. This epoch is particularly long for the low-B_{dip}, low-P_0 models and short for the high-B_{dip} models; this trend in behaviour leads to the field strength turnover in heavy element nucleosynthesis, as discussed in Section 3.

(from the temperature and density trends, respectively), shorter rotation periods are more conducive to heavy element nucleosynthesis (in agreement with Vlasov et al. 2017). Additionally, Fig. 5 highlights that at $t_{\mathrm{E,\,max}}$, rotators with $P_0 = 1.5$ ms synthesize heavy elements in large mass fractions, compared to similar configurations.

Since the IC times tested here are B_{dip} and P_0 dependent, they vary significantly depending on our protomagnetar parameter choices. This difference in IC time between t_{bo} and $t_{\gamma,\,\mathrm{dis}}$ further drives a transition in the trends of B_{dip}; at IC times before $t_{\gamma,\,\mathrm{dis}}$, a smaller field strength results in a higher $\overline{A}$, while after t_{bo} this trend is reversed. This is supported in Fig. 6, where we see that the low-field strength models have the largest difference between these IC times. This time window contributes to the decrease in ρ and T, i.e. ρ and T decrease more between t_{bo} and $t_{\gamma,\,\mathrm{dis}}$ for low-field strength models and less for high-field models. Since the initial densities and temperatures are somewhat predictive of the trends in $\overline{A}$, we have this transition.

Changing Y_e gives expected results: neutron-rich outflows lead to greater heavy element nucleosynthesis than proton-rich outflows. This variation in Y_e naturally sets the scale of $\overline{A}$ and leads to monotonic trends in electron fraction.

Interestingly, the qualitative trends change somewhat if we discuss $\overline{A}$ as a function of the model parameter space, but exclude the contribution from free neutrons, protons, and helium nuclei. Since these light nuclei make up the majority of the mass synthesized in proton-rich conditions and later IC times, excluding them allows us to focus on the trends seen in higher A nuclei. For example, $\overline{A}$ is an especially useful measure for cosmic ray physics, but does not say much about the distribution of the abundance pattern created. In some configurations, elements up to and exceeding the third r-process peak are created, but in negligible amounts by mass fraction. These nuances are more readily captured by excluding protons, neutrons, and helium nuclei, which we denote by $\overline{A}_{\mathrm{heavy}}$. Fig. 7 shows the subfigures along the diagonal of Fig. 5 but expressed instead with $\overline{A}_{\mathrm{heavy}}$. This diagonal shows some of the general features of $\overline{A}_{\mathrm{heavy}}$ as a function of the model parameters, but is not as purely monotonic as the $\overline{A}$ plot and has several exceptions. Similar to the trends in $\overline{A}$, initial spin period generally has a greater effect than magnetic field strength for $\overline{A}_{\mathrm{heavy}}$. At early IC times (with the exception of $Y_e = 0.55$), $\overline{A}_{\mathrm{heavy}}$ has an inverse magnetic field strength-initial spin relation. Most of the mass for the high period configurations goes into free nucleons and helium, driving a lower P_0 preference in $\overline{A}$, but in terms of $\overline{A}_{\mathrm{heavy}}$, a higher P_0 leads to more massive nuclei. At late IC times (with the exception of $Y_e = 0.55$), $\overline{A}_{\mathrm{heavy}}$ peaks in a band between $P_0 \sim 2{-}3$ ms, as shown in the third panel of Fig. 7. The trends in Y_e and IC time are strictly not monotonic. In neutron-rich conditions ($Y_e = 0.45,\ 0.475$), a lower electron fraction leads to heavier nucleosynthesis – as with $\overline{A}$. The lowest values of $\overline{A}_{\mathrm{heavy}}$ are reached in proton-rich conditions ($Y_e = 0.55$) and this trend is also present in $\overline{A}$. However, when the electron fraction is maintained at 0.5, much higher mass numbers can be synthesized (due to the process described earlier from Meyer 2002). In IC time, generally the most nucleosynthesis occurs at photodisintegration time ($t_{\gamma,\,\mathrm{dis}}$), and $\overline{A}_{\mathrm{heavy}}$ decreases both before and after. Finally, at $Y_e = 0.55$, the trends in time, B_{dip}, and P_0 generally agrees with the trends of $\overline{A}$, but at higher mass numbers.

Note that the rigid changes in the contour curves are not necessarily a feature of the numerical analysis. They are a result of a simple order-one interpolation on the 30 $B_{\mathrm{dip}} - P_0$ configurations presented here; adding additional data points would improve the resolution and, thus, the smoothness of the figures. Nevertheless, the qualitative conclusions discussed here should remain valid.

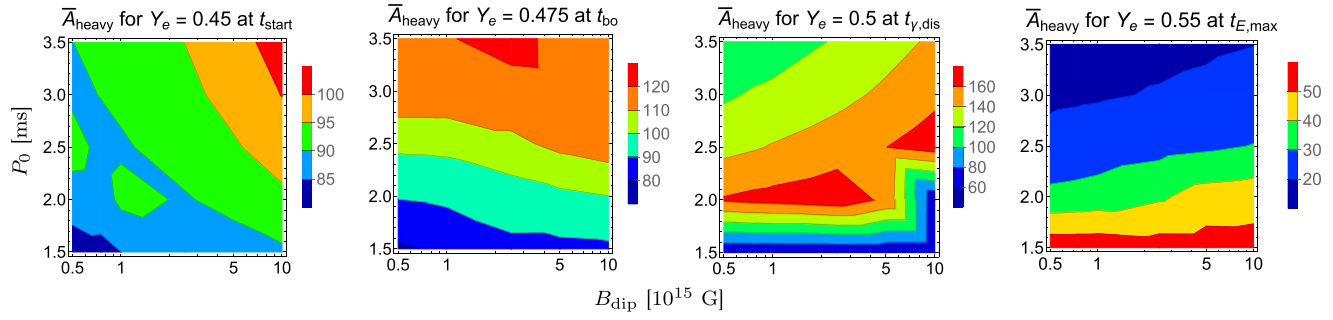

Figure 7. Contours of mean mass number calculated after excluding free nuclei and helium isotopes, $\overline{A}_{\mathrm{heavy}}$. This provides a useful measure of the distribution in abundance of heavy elements since much of the mass contributing to $\overline{A}$ comes from free nucleons and helium. The figures are shown for a diagonal section of Fig. 5: four IC times and at four electron fractions to quantify most of the trends, although they are not so monotonic and each have exceptions. Note that the colour range in each figure is different.

4 DISCUSSION

We first discuss the trends in model parameter space that explain the conditions conducive to heavy element synthesis, explore the validity of the parameter range, and describe the validity of other assumptions made in this work.

Magnetic field trends and considerations: At early IC times (start and breakout times), a lower magnetic field is more conducive to heavy element nucleosynthesis. The low-magnetic field yields initial outflow densities that are higher than those for high-magnetic field configurations; slower expansions and high mass-loss rates initially enhance the neutron-capture rate and suggest the synthesis of heavier elements. The transition between a preference of the low-$B_{\rm dip}$ and high-$B_{\rm dip}$ models is driven by the transition in preference of the mass-loss rate. This is, in turn, caused by increased magnetocentrifugal slinging for high-$B_{\rm dip}$ models after $t_{\rm bo}$. This is true regardless of the choice of Y_e and P_0 (except in the case for the fastest rotators, with $P_0 = 1.5$ ms).

Given that the later IC times (photodisintegration and max acceleration times) are generally more relevant for UHECR implications, it seems that the higher magnetic field configurations are more important for heavy element nucleosynthesis (with the notable exception of $B_{\rm dip} = 5 \times 10^{14}$ G and $P_0 = 1.5$ ms). However, we do not time-integrate $\overline{A}$ nor do we consider additional photodisintegration interactions as the nuclei make their way out of the star and are accelerated. It may turn out, then, that the protomagnetars with low/moderate $B_{\rm dip}$ are important as well, since some amount of the heavy nuclei synthesized between $t_{\rm bo}$ and $t_{\gamma,\,\rm dis}$ are only partially photodisintegrated. Finally, the variation in magnetic field strength has a weaker effect on the final $\overline{A}$ compared to the variation in initial spin period at all IC times.

The range of magnetic field strengths considered here should be a representative sample of the possible stable field strengths. For example, magnetic field strengths of order $\sim 10^{17}$ G can be reached if the magnetic energy in the dipole field is approximately equal to the rotational energy. However, stable field configurations require a total magnetic field strength at least 10 times larger than the dipole component, which results in a dipole field strength of $\sim 10^{16}$ G (Metzger et al. 2011a). We can also look at recent observations to inform us on the magnetic field and spin periods of millisecond magnetars. Multiple recent works have shown that millisecond magnetar central engines can give rise to long-duration GRBs (see e.g. Lü & Zhang 2014; Yi et al. 2014; Rea et al. 2015). The values chosen here fit reasonably well within the range of beam-corrected dipolar magnetic field strengths inferred from these studies. Below $\sim 10^{14}$ G, the PNS is no longer generally considered a protomagnetar. Also, mildly magnetized pulsars may not have the collimation power to produce jets that break through the stellar material; for example, in the mild magnetic field scenarios studied in Fang et al. (2012), particle acceleration occurs in the vicinity of the compact object and therefore hadronuclear interactions as nuclei escape from the supernova remnant significantly reduce the final nuclear composition.

Initial spin period trends and considerations: At all times and Y_e, an increasing period yields decreased heavy element nucleosynthesis. Initial spin period, P_0 is more dominant with regard to $\overline{A}$ synthesized than the field strength is. P_0 has such an important impact because of its effect on the magnetic field structure and the fraction of the PNS surface threaded by the open magnetic field lines (i.e. in the correction factor $f_{\rm open}$). There is $\sim$2 times more variation in $f_{\rm open}$ over the range of P_0 values compared to the range of $B_{\rm dip}$ values chosen here. This gives a decreased density which correlates with a decreased $\overline{A}$. Further, and more importantly, as P_0 increases, entropy increases by a factor $\gtrsim 2$. The larger entropy increases the temperature, resulting in more photodisintegration during the nucleosynthesis epoch and lower $\overline{A}$ values.

These initial spin period trends may break down for $P_0 \leq 1$ ms. Although spin period is treated as an independent parameter in this study, it is coupled to the electron fraction, the mass-loss rate, and the overall stability of the neutron star (e.g. Strobel, Schaab & Weigel 1999; Metzger et al. 2008, 2011a). At initial spin periods greater than 3.5 ms, these trends are likely to continue monotonically (see also Vlasov et al. 2017 for trends in protomagnetar spin period and Bhattacharya et al. 2021 for analysis up to 5 ms). Furthermore, we can look at the X-ray plateau data for long-duration GRBs (Lü & Zhang 2014; Yi et al. 2014; Rea et al. 2015), to see that the P_0 range chosen here fits well within the inferred, beam-corrected spin periods assuming a magnetar central engine.

IC time trends and considerations: Earlier times post-core-collapse are more favourable for the synthesis of heavy elements; the initial time and breakout times yield similar results. After breakout time, there is a more significant drop in the ability for the magnetar outflow to synthesize heavy elements. At later times relevant for sourcing UHECR (between photodisintegration time and max acceleration times), rapid rotators could create large quantities of intermediate/heavy mass nuclei, but only under neutron-rich conditions.

However, some fraction of heavy elements should survive photodisintegration between $t_{\rm bo}$ and $t_{\gamma,\,\rm dis}$ to be important for UHECR considerations. Since, this time difference (Fig. 6) is parameter dependent, it may turn out that the low-$B_{\rm dip}$ configurations are still more important for heavy element survival if partial survival is taken into account. This analysis is left for future work.

As previously mentioned, between the early and late IC times, a transition occurs where high-$B_{\rm dip}$ protomagnetars are better at synthesizing heavier nuclei. Finally, at IC times later than $t_{\rm E,\,max}$, the outflows would be dominated by free neutrons, protons, and helium nuclei, although the mass ejected is much lower at such late times.

Y_e trends and considerations: Overall heavy nucleosynthesis depends monotonically on the choice of Y_e; in terms of the mean mass number (and fraction above iron), $\overline{A}_{Y_e=0.45} > \overline{A}_{Y_e=0.475} > \overline{A}_{Y_e=0.5} > \overline{A}_{Y_e=0.55}$. In neutron-rich conditions ($Y_e = 0.45, 0.475$), large fractions of heavy elements are created. As soon as there are equal parts of neutrons and protons, there is a noticeable drop in the amount of heavy elements synthesized (see the change in slope past $Y_e = 0.5$ in Fig. 4).

Although it is not explored in this work, it is expected that under even more neutron rich conditions ($Y_e \lesssim 0.4$), we would see a higher $\overline{A}$ and X_h. In order to reach significant amounts of third r-process peak nuclei, studies suggest $Y_e \lesssim 0.25$ is required (Kasen, Fernández & Metzger 2015; Lippuner & Roberts 2015). In this study, we adopt a range of Y_e that may represent more typical values for magnetorotational CCSNe (see numerical simulations of Vlasov et al. 2017, Grimmett et al. 2020, and Reichert et al. 2021), but in rarer cases, e.g. where the rotation period is less than 1 ms, Y_e at the base of the outflow may be significantly lower and reach $\sim$0.1−0.3 (Metzger et al. 2008; Winteler et al. 2012). In general, under more proton-rich conditions ($Y_e \gtrsim 0.6$), it is expected that we would see less heavy element synthesis (although the νp-process could induce interesting departures).

Finally, we hold Y_e fixed throughout the thermodynamic trajectories given that there is a degree of uncertainty in its dynamical evolution for the magnetized outflows considered here. With that in mind, choosing to test a range in electron fraction, $0.45 \leq Y_e \leq 0.55$

allows us to understand the important trends in Y_e and with a given Y_e trajectory, we are also able to make qualitative statements on the composition.

Other considerations: For this study, we fix the PNS mass to $1.4\,M_\odot$ and magnetic obliquity angle to $\pi/2$. A higher PNS mass leads to an elevated energy loss rate, but a smaller σ_0 and $\tau_{\rm exp}$ which generally leads to less nucleosynthesis. At early times post-CC, this can result in up to a ~ 20 per cent decrease in X_h, but becomes marginal at late times (Bhattacharya et al. 2021). The magnetic field of the PNS can also play a role in baryon loading of the outflow, the amount of mass ejected (see e.g. Shibata et al. 2011), and therefore its heavy element yield, but in this work, we assume the neutrino-driven wind mass-loss of Metzger et al. (2011a) as the dominant mechanism. Changes in the magnetic obliquity angle can also have significant implications for the nucleosynthesis products of these outflows (see Halevi & Mösta 2018, up to a ~ 40 per cent difference in X_h at early times post-CC in Bhattacharya et al. 2021). Decreasing this angle tends to reduce the amount of entropy suppression in the outflow (in the case of Bhattacharya et al. 2021, Fig. 7, this results in decreased heavy element nucleosynthesis). Increased heating near the seed formation radius, however, may increase the neutron-to-seed ratio and improve nucleosynthesis (see Vlasov et al. 2017 for discussion of aligned versus misaligned rotators).

We also evolve $\dot{M}$, S, $\tau_{\rm exp}$, and other outflow properties in IC time, but consider them as fixed parameters in Outflow time for our thermodynamic trajectories. We do not expect these to strongly affect the products of nucleosynthesis, since these quantities do not change appreciably in the nucleosynthesis time-scale (~ 10 ms, see Fig. 2). With these assumptions, we can still extract some important results in terms of the magnetar model parameters. To estimate the outflow radius as a function of time and jet magnetization, we adopt the magnetic reconnection model of Drenkhahn & Spruit (2002; see Fig. 1 for the radial trajectories). However, the dissipation process need not be continuous within the outflow and is model dependent. Other descriptions, such as the turbulent reconnection models of Zhang & Yan (2010) and Lazarian, Zhang & Xu (2019), could yield different results for the time-dependent thermodynamic quantities derived here, but the extent of this difference is unclear. These alternative models also have important implications for the acceleration and photodisintegration of the nuclei via, e.g. the GRB photon spectrum. Thus, an investigation of the effects of the dissipation model on the composition and subsequent evolution is warranted.

`SkyNet` requires an initial abundance pattern, along with thermodynamic trajectories and other input parameters, to evolve the network and calculate the abundance patterns over time. In order to determine this initial abundance pattern, we make use of the NSE evolution mode, which requires only the initial density, temperature, and electron fraction. The majority of all outflows studied here begin with temperatures comfortably above the ~ 7 GK NSE threshold for full network evolution, meaning that for most configurations, this initial abundance pattern created by `SkyNet` is effectively made up of free nucleons determined by the electron fraction. However, at $t_{\rm E,\,max}$, some low $B_{\rm dip}$ and $P_0 = 1.5$ ms configurations have initial temperatures below 7 GK.

For these $P_0 = 1.5$ ms cases at $t_{\rm E,\,max}$, the lower temperatures result in initial abundance patterns that are not quite in NSE; the free nucleons are in equilibrium with some amount of heavier elements. This process is similar to the NSE and 'quasi-nuclear equilibrium' (QSE) results, e.g. Wanajo et al. (2018), where, as temperatures cool, NSE/QSE result in equilibrium of free nucleons and iron group elements (see also Bodansky, Clayton & Fowler 1968 and Meyer, Krishnan & Clayton 1998 relating to silicon burning reactions). This results in initial fractions of heavy elements that are far greater than those of other configurations where the temperature is higher. These are similar methods to those of Roberts et al. (2016) and Lippuner & Roberts (2017) where the NSE evolution mode also calculates the initial abundance, despite an initial temperature of ~ 6 GK, below the network threshold.

Finally, while $\overline{A}$ is a good measure for cosmic rays and descriptive of what most of the mass is synthesized into, $\overline{A}_{\rm heavy}$ is more descriptive of the abundance distributions in each model configuration. In magnetic field strength and initial spin period, the trends are inverted, i.e. at early IC times, the highest mass numbers are synthesized for high $B_{\rm dip}$-high P_0 configurations for $Y_e = 0.45,\ 0.475,$ and 0.5. At late IC times, however, the highest mass numbers are synthesized in a band around $\sim$2−3 ms spin periods. $\overline{A}_{\rm heavy}$ in terms of Y_e is ordered as $\overline{A}_{\rm heavy,Ye=0.55} < \overline{A}_{\rm heavy,Ye=0.45} < \overline{A}_{\rm heavy,Ye=0.475} < \overline{A}_{\rm heavy,Ye=0.5}$. In the case of $Y_e = 0.5$ at later IC times, very massive nuclei are synthesized. In the case of $Y_e = 0.55$, the trends tend not to change, but higher mass numbers are reached compared to $\overline{A}$. There are several exceptions to these rules, however.

5 SUMMARY AND CONCLUSION

We performed a numerical study of the nucleosynthesis of proto-magnetar outflows to systematically probe the conditions suitable for heavy element nucleosynthesis. We adopted a parametrized model for the protomagnetar in terms of physical and dynamical properties of the magnetar and its outflows. Our results can be summarized as:

(i) *Heavy elements* ($\overline{A} \sim 20 - 65$) are generally synthesized only in neutron-rich conditions ($Y_e < 0.5$) for the more rapid rotators ($P_0 \lesssim 2.5$ ms). In these conditions, earlier IC times ($t_{\rm start}$ and $t_{\rm bo}$) are more conducive for heavy elements and there is a generally weak dependence on $B_{\rm dip}$. This represents a smaller subspace of the total parameter space and is subjected to composition-altering photodisintegration at the dissipation radius. This population could be described as an intermediate composition after the epoch of particle acceleration, depending on photodisintegration details.

(ii) *Lighter elements* ($\overline{A} \sim 10 - 50$) are synthesized under a broader set of conditions than heavy elements. These elements are synthesized still under neutron-rich conditions (and in some cases, under proton-rich conditions), but also at the later IC times ($t_{\gamma,\,\rm dis}$ and $t_{\rm E,\,max}$) where photodisintegration will no longer substantially alter the composition and nuclei can still be accelerated to ultra-high energies. This also generally occurs only for the more rapid rotators with a weak dependence on the magnetic field strength.

(iii) *Limited synthesis* ($\overline{A} \sim 4 - 15$) occurs for $Y_e \geq 0.5$. If the outflow is launched at $t_{\gamma,\,\rm dis}$ or $t_{\rm E,\,max}$ and $P_0 \gtrsim 3$ ms, even neutron-rich outflows produce light elements.

These trends suggest that the overall outflow composition from a protomagnetar could be dominated by light, intermediate, or heavy nuclei, but depends sensitively on the spin period and time evolution of the electron fraction. Nuclei around the third *r*-process peak are not typically reached, even in the most favourable conditions considered here (low $B_{\rm dip}$, low P_0, $Y_e = 0.45$, at $t_{\rm start}$). Some amount of first and second *r*-process peak elements are produced in these favourable conditions, so protomagnetars may be a contributor to the weak *r*-process abundance.

To fully understand the contribution of magnetar central engines to the entire UHECR flux requires an improved understanding of the population and distribution of such sources, both theoretical and observational. Additionally, improved understanding of the acceleration, propagation, and survival of nuclei will be important.

This paper supports a growing notion of intermediate mass UHECR composition in certain magnetar model configurations.

It remains to be seen how the composition (and abundance distribution) changes when integrated over time and weighted by the distribution of magnetar properties in the whole population. After nucleosynthesis, processes such as disintegration, acceleration, and propagation must be considered if sites like these are to contribute significantly to the UHECR spectrum. Uncertainties in features like the extragalactic magnetic field will be coupled to the composition of heavy nuclei that are synthesized near the source. Each stage requires further study and is left for future work.

ACKNOWLEDGEMENTS

We thank Kohta Murase, David Radice, and Yudai Suwa for useful discussions. We thank Ke Fang, Kunihito Ioka, Brian Metzger, Bing Theodore Zhang, and the anonymous reviewer for carefully reading the manuscript and providing insightful suggestions that helped improve the paper. NE and MB are supported by NSF Grant No. PHY-1914409. MB acknowledges support from Eberly Research Fellowship at the Pennsylvania State University. The work of SH is supported by the U.S. Department of Energy Office of Science under award number DE-SC0020262, NSF Grant Nos AST1908960 and PHY-1914409, and JSPS KAKENHI Grant Number JP22K03630. This work was supported by World Premier International Research Center Initiative (WPI Initiative), MEXT, Japan.

DATA AVAILABILITY

The data underlying this article will be shared on reasonable request to the corresponding author.

REFERENCES

Aab A. et al., 2014a, Phys. Rev. D, 90, 122005
Aab A. et al., 2014b, Phys. Rev. D, 90, 122006
Aab A. et al., 2014c, ApJ, 794, 172
Aab A. et al., 2015a, ApJ, 804, 15
Aab A. et al., 2015b, Nucl. Instrum. Methods A, 798, 172
Aab A. et al., 2017, Science, 357, 1266
Aab A. et al., 2018, ApJ, 853, L29
Abbasi R. et al., 2009, Astropart. Phys., 32, 53
Abbasi R. U. et al., 2018, ApJ, 858, 76
Abbott B. P. et al., 2017, ApJ, 850, L39
Abreu P. et al., 2010, Astropart. Phys., 34, 314
Abu-Zayyad T. et al., 2013, ApJ, 768, L1
Alves Batista R. et al., 2019, Front. Astron. Space Sci., 6, 23
Anchordoqui L. A., 2019, Phys. Rep., 801, 1
Arcones A., Montes F., 2011, ApJ, 731, 5
Arnould M., Goriely S., Takahashi K., 2007, Phys. Rep., 450, 97
Arons J., 2003, ApJ, 589, 871
Batista R. A., de Almeida R. M., Lago B., Kotera K., 2019, JCAP, 2019, 002
Bhattacharya M., Horiuchi S., Murase K., 2021, preprint (arXiv:2111.05863)
Biermann P. L. et al., 2016, preprint (arXiv:1610.00944)
Bliss J., Arcones A., Montes F., Pereira J., 2017, J. Phys. G: Nucl. Part. Phys., 44, 054003
Bodansky D., Clayton D. D., Fowler W. A., 1968, ApJS, 16, 299
Bromberg O., Granot J., Piran T., 2015, MNRAS, 450, 1077
Chen M.-H., Li L.-X., Lin D.-B., Liang E.-W., 2021, ApJ, 919, 59
Côté B. et al., 2018, ApJ, 855, 99
Cybert R. H. et al., 2010, ApJS, 189, 240
Drenkhahn G., 2002, A&A, 387, 714
Drenkhahn G., Spruit H. C., 2002, A&A, 391, 1141
Duncan R. C., Thompson C., 1992, ApJ, 392, L9
Fang K., Kotera K., Olinto A. V., 2012, ApJ, 750, 118
Fröhlich C., Martínez-Pinedo G., Liebendörfer M., Thielemann F.-K., Bravo E., Hix W. R., Langanke K., Zinner N. T., 2006, Phys. Rev. Lett., 96, 142502
Fujibayashi S., Yoshida T., Sekiguchi Y., 2016, ApJ, 818, 96
Greisen K., 1966, Phys. Rev. Lett., 16, 748
Grimmett J. J., Müller B., Heger A., Banerjee P., Obergaulinger M., 2020, MNRAS, 501, 2764
Halevi G., Mösta P., 2018, MNRAS, 477, 2366
Hillas A. M., 2005, J. Phys. G Nucl. Phys., 31, R95
Hix W., Thielemann F.-K., 1999, J. Comput. App. Math., 109, 321
Hoffman R. D., Woosley S. E., Qian Y., 1997, ApJ, 482, 951
Horiuchi S., Murase K., Ioka K., Mészáros P., 2012, ApJ, 753, 69
Jiang Y., Zhang B. T., Murase K., 2021, Phys. Rev. D, 104, 043017
Kasen D., Fernández R., Metzger B. D., 2015, MNRAS, 450, 1777
Khan E., Goriely S., Allard D., Parizot E., Suomijärvi T., Koning A., Hilaire S., Duijvestijn M., 2005, Astropart. Phys., 23, 191
Kotera K., 2011, Phys. Rev. D, 84, 023002
Kotera K., Olinto A. V., 2011, ARA&A, 49, 119
Kuznetsov M., Tinyakov P., 2021, JCAP, 2021, 065
Kyutoku K., Ioka K., 2016, ApJ, 827, 83
Lamers H. J. G. L. M., Cassinelli J. P., 1999, Introduction to Stellar Winds. Cambridge Univ. Press, Cambridge
Lazarian A., Zhang B., Xu S., 2019, ApJ, 882, 184
Lemoine M., Waxman E., 2009, JCAP, 2009, 009
Lippuner J., Roberts L. F., 2015, ApJ, 815, 82
Lippuner J., Roberts L. F., 2017, ApJS, 233, 18
Lü H.-J., Zhang B., 2014, ApJ, 785, 74
M'osta P., Roberts L. F., Halevi G., Ott C. D., Lippuner J., Haas R., Schnetter E., 2018, ApJ, 864, 171
Margutti R. et al., 2013, ApJ, 778, 18
Margutti R. et al., 2014, ApJ, 797, 107
Metzger B. D., Thompson T. A., Quataert E., 2007, ApJ, 659, 561
Metzger B. D., Thompson T. A., Quataert E., 2008, ApJ, 676, 1130
Metzger B. D., Giannios D., Thompson T. A., Bucciantini N., Quataert E., 2011a, MNRAS, 413, 2031
Metzger B. D., Giannios D., Horiuchi S., 2011b, MNRAS, 415, 2495
Meyer B. S., 2002, Phys. Rev. Lett., 89, 231101
Meyer B. S., Krishnan T. D., Clayton D. D., 1998, ApJ, 498, 808
Mumpower M. R., Kawano T., Ullmann J. L., Krticka M., Sprouse T. M., 2017, Phys. Rev. C, 96, 024612
Murase K., Ioka K., Nagataki S., Nakamura T., 2008, Phys. Rev. D, 78, 023005
Nagataki S., Kohri K., 2001, PASJ, 53, 547
Pons J. A., Reddy S., Prakash M., Lattimer J. M., Miralles J. A., 1999, ApJ, 513, 780
Qian Y., Woosley S. E., 1996, ApJ, 471, 331 (QW96)
Rea N., Gullón M., Pons J. A., Perna R., Dainotti M. G., Miralles J. A., Torres D. F., 2015, ApJ, 813, 92
Reichert M., Obergaulinger M., Eichler M., Aloy M. A., Arcones A., 2021, MNRAS, 501, 5733
Roberts L. F., Woosley S. E., Hoffman R. D., 2010, ApJ, 722, 954
Roberts L. F. et al., 2016, MNRAS, 464, 3907
Rodrigues X., Heinze J., Palladino A., van Vliet A., Winter W., 2021, Phys. Rev. Lett., 126, 191101
Shibata M., Suwa Y., Kiuchi K., Ioka K., 2011, ApJ, 734, L36
Skuladottir A. et al., 2021, ApJ, 915, L30
Sneden C., Cowan J. J., Gallino R., 2008, Ann. Rev. Astron. Astrophys., 46, 241
Strobel K., Schaab C., Weigel M. K., 1999, A&A, 350, 497
Surman R., Mumpower M., Sinclair R., Jones K. L., Hix W. R., McLaughlin G. C., 2014, AIP Adv., 4, 041008
Telescope Array Collaboration, 2015, preprint (arXiv:1511.02103)
The Pierre Auger Collaboration, 2019, preprint (arXiv:1909.09073)
Thompson T. A., Burrows A., Meyer B. S., 2001, ApJ, 562, 887
Thompson T. A., Chang P., Quataert E., 2004, ApJ, 611, 380
Timmes F. X., Douglas Swesty F., 2000, ApJS, 126, 501
Unger M., Farrar G. R., Anchordoqui L. A., 2015, Phys. Rev. D, 92, 123001

Usov V. V., 1992, Nature, 357, 472
Vlasov A. D., Metzger B. D., Lippuner J., Roberts L. F., Thompson T. A., 2017, MNRAS, 468, 1522
Wanajo S., Müller B., Janka H.-T., Heger A., 2018, ApJ, 852, 40
Wheeler J. C., Yi I., Hoflich P., Wang L., 2000, ApJ, 537, 810
Winteler C., 2014, PhD thesis, Univ. Basel
Winteler C., Käppeli R., Perego A., Arcones A., Vasset N., Nishimura N., Liebendörfer M., Thielemann F. K., 2012, ApJ, 750, L22
Yi S. X., Dai Z. G., Wu X. F., Wang F. Y., 2014, preprint (arXiv:1401.1601)
Yong D. et al., 2021, Nature, 595, 223
Zatsepin G. T., Kuz'min V. A., 1966, Soviet J. Exp. Theo. Phys. Lett., 4, 78
Zhang B. T., Murase K., Kimura S. S., Horiuchi S., Mészáros P., 2018, Phys. Rev. D, 97, 083010
Zhang B., Mészáros P., 2001, ApJ, 552, L35
Zhang B., Yan H., 2010, ApJ, 726, 90

APPENDIX A: NOTATION TABLE

We include a table of the symbols that we use, their physical description, and the first equation/section where they are used in ('Text' if the symbol comes from within the text). In some cases, the first equation is not the best location for the symbol; for instance, $\dot{M}$ is first mentioned in equation (1) but equation (6) is used for computing the thermodynamic trajectories with `SkyNet`.

Table A1. Symbol, description, and first location (equation and/or section) of the symbol for the variables used in this paper. For the symbols from equations in text, 'Text' is used.

Symbol	Description	1st Equation / Section
$\dot{M}$	Mass-loss rate from neutrino-driven outflows.	(1) / Section 2.1
r	Radial coordinate of the outflow.	(1) / Section 2.1
ρ	Outflow density.	(1) / Section 2.1
v	Outflow velocity at radial coordinate.	(1) / Section 2.1
$f_{\rm open}$	Fraction of magnetosphere open to outflows.	(1) / Section 2.1
$f_{\rm cent}$	Fractional mass-loss rate from magnetocentrifugal slinging.	(1) / Section 2.1
S	Entropy per baryon.	(2) / Section 2.1
T	Temperature of the outflow.	(2) / Section 2.1
$\tau_{\rm exp}$	Expansion time-scale, used as IC.	(3) / Section 2.1
$T_{\rm rec}$	Recombination temperature.	(3) / Section 2.1
χ	Obliquity angle: angle between magnetic field and rotation axes.	Text / Section 2.1
$R_{\rm NS}$	Neutron star radius.	Text / Section 2.1
R_Y	'Y'-point radius: final radius where magnetic field lines are still closed.	Text / Section 2.1
$f_{\rm cent,\,max}$	Maximum centrifugal slinging correction.	Text / Section 2.1
R_A	Alfven radius.	Text / Section 2.1
R_S	Sonic radius.	Text / Section 2.1
R_L	Light cylinder radius.	Text / Section 2.1
Ω	Neutron star rotation rate.	Text / Section 2.1
$P_{\rm cent}$	Period factor accounting for centrifugal effects of rapid rotation.	Text / Section 2.1
α	Argument to determine inclination angle	Text / Section 2.1
$M_{\rm NS}$	Neutron star baryonic mass.	Text / Section 2.1
$\theta_{\rm open}$	Opening angle of the polar cap.	Text / Section 2.1
$C_{\rm es}$	Heating correction factor for neutrino-electron scattering.	(6) / Section 2.1
L_ν	Neutrino luminosity for $\overline{\nu}_e$ (anti-electron flavour).	(6) / Section 2.1
ϵ_ν	Mean neutrino energy for $\overline{\nu}_e$ (anti-electron flavour).	(6) / Section 2.1
R_{10}	NS radius divided by 10 km.	(6) / Section 2.1
$M_{1.4}$	$M_{\rm NS}$ divided by 1.4 solar masses.	(6) / Section 2.1
η_s	A 'stretch' factor to correct neutrino quantities for rotation.	Text / Section 2.1
$S_{\rm rot}$	Entropy suppressed by rapid rotation.	Text / Section 2.1
β_j	Unit-less jet velocity.	(9) / Section 2.2
Γ_j	Jet Lorentz factor.	(9) / Section 2.2
σ_0	Outflow magnetization, corresponds to maximum Lorentz factor.	(9) / Section 2.2
$R_{\rm mag}$	Magnetic saturation radius.	(9) / Section 2.2
ϕ	Magnetic flux threading open magnetosphere.	(11) / Section 2.2
$t_{\rm bo}$	Jet breakout time; when outflow breaks out of progenitor envelope.	(12) / Section 2.2
$B_{\rm dip}$	Surface dipolar magnetic field strength.	(12) / Section 2.2
P_0	Initial spin period.	(12) / Section 2.2
$\tau_{\gamma-N}$	The number of nuclei-destroying interactions.	(13) / Section 2.2
$t_{\rm E,\,max}$	Last time when nuclei can be accelerated above 10^{20} eV.	Text / Section 2.2
$\dot{E}_{\rm iso}$	Isotropic jet luminosity.	(13) / Section 2.2
$\varepsilon_{\rm rad}$	Radiative efficiency of the jet.	(13) / Section 2.2
C	Fraction of gamma-ray photons released below Band peak energy.	(13) / Section 2.2
$\sigma_{\rm GDR}$	Resonance cross-section.	(13) / Section 2.2
$\overline{\epsilon}_{\rm GDR}$	Resonance energy.	(13) / Section 2.2
$\Delta\epsilon_{\rm GDR}$	Resonance width.	(13) / Section 2.2
ϵ_p	Band peak energy.	(13) / Section 2.2

Table A1 – *continued*

Symbol	Description	1st Equation / Section
A	Mass number.	Text / Section 2.2
Y_e	Electron fraction.	Text / Section 2.3
n_p	Proton number density.	Text / Section 2.3
n_n	Neutron number density.	Text / Section 2.3
$t_{\rm start}$	Time after core collapse when magnetar outflow begins.	Text / Section 2.3
$t_{\gamma,\,\rm dis}$	When synthesized nuclei will no longer be photodisintegrated.	Text / Section 2.3
Y	Abundance of nuclei.	Text / Section 3.1
Z	Charge number.	Text / Section 3.1
$\overline{A}$	Mean mass number, weighted by abundance.	(14) / Section 3.2
X_h	Total mass fraction of elements more massive than iron.	(15) / Section 3.2
X	Mass fraction.	(15) / Section 3.2
$\overline{A}_{\rm heavy}$	Mean mass number excluding free nuclei and helium.	Text / Section 3.2

APPENDIX B: INITIAL CONDITIONS

The ICs for each numerical test ultimately determine the final abundance pattern. None of these ICs directly determine the final abundance pattern, but, from SkyNet's perspective, is rather a competition between the thermodynamic trajectories of density, temperature, and electron fraction over time. These trajectories are necessarily coupled to the entropy, expansion time-scale, mass-loss rate, etc. So while a direct correlation of ICs do not tell the full story, the initial densities and temperatures are somewhat indicative of the final results.

Here, we summarize some features and general trends from the ICs:

(i) Initial density, temperature, and mass-loss rate show a transition in $B_{\rm dip}$ preference between $t_{\rm bo}$ and $t_{\gamma,\,\rm dis}$.

(ii) ρ and T have regions that are not purely monotonic (ρ at $t_{\gamma,\,\rm dis}$ and $t_{\rm E,\,max}$ and T at $t_{\rm bo}$).

(iii) Entropy is a function of spin period, but not directly a function of field strength. The field strength dependence at later IC times arises from the IC dependence on field strength and spin period.

(iv) The $B_{\rm dip}$ and P_0 trends in $\tau_{\rm exp}$ and $\dot{M}$ are reflective of the magnetic field and spin period trends of the $f_{\rm open}$ and $f_{\rm cent}$ correction factors.

(v) Overall, ρ and T (and, to a lesser degree, $\dot{M}$) may be indicative of the $B_{\rm dip}$ and IC time nucleosynthesis trends: generally, higher densities suggest higher values of $\overline{A}$ and higher temperatures suggest lower values of $\overline{A}$, but do not directly predict the results.

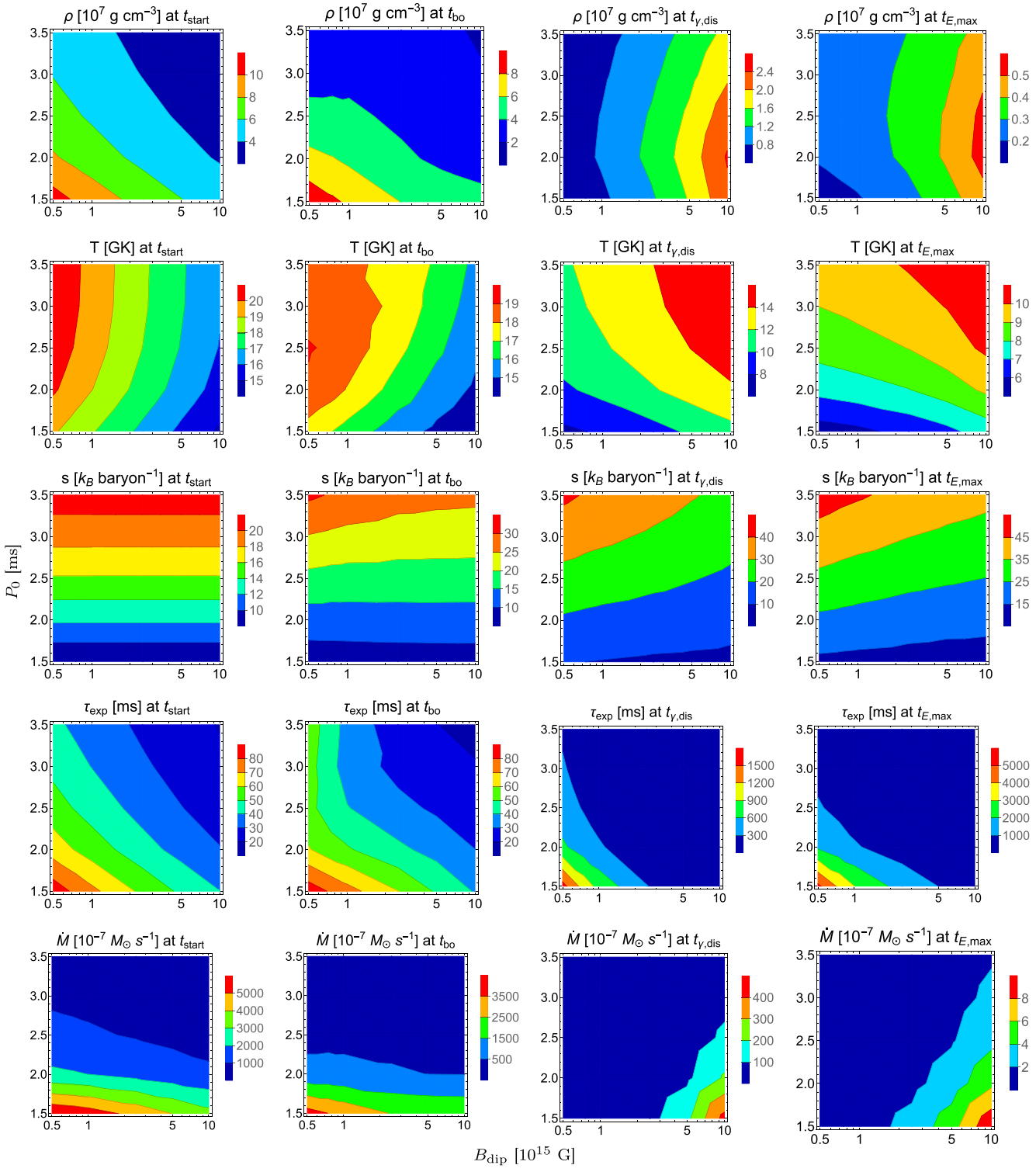

Figure B1. Top-to-bottom: The contours for the initial outflow conditions; density, temperature, entropy per baryon, expansion time-scale, and mass-loss rate are shown. Left-to-right: The figure panels are ordered by the IC time. Note the transition in $B_{\rm dip}$ trends for ρ, T, and $\dot{M}$, that is suggestive of the final trends in $\overline{A}$.

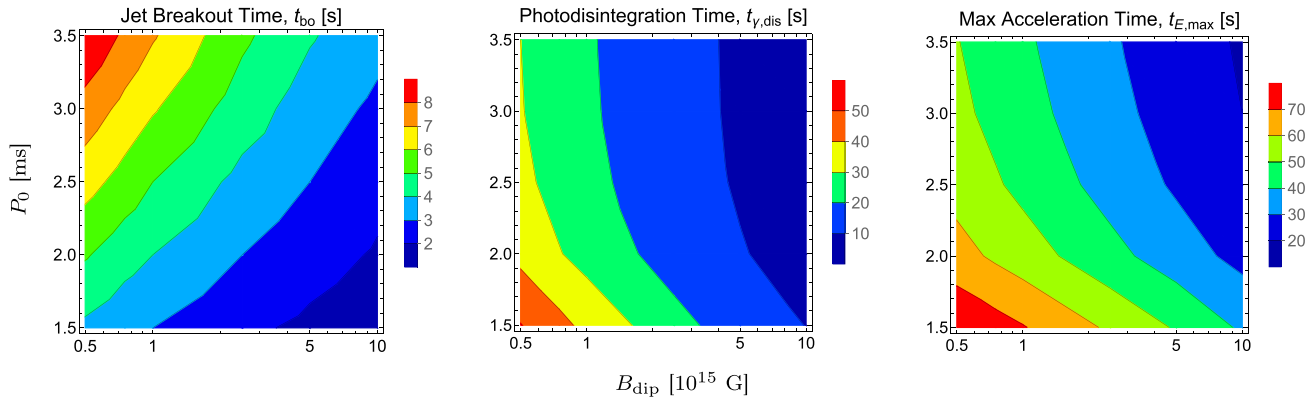

Figure B2. Left-hand panel: Breakout time as a function of B_{dip} and P_0. Middle panel: Photodisintegration time, i.e. when $\tau_{\gamma-N} \sim 1$ as a function of B_{dip} and P_0. Right-hand panel: Max acceleration IC time, i.e. the time when particles can no longer be accelerated above $E_{max} = 10^{20}$ eV as a function of B_{dip} and P_0.

APPENDIX C: ANALYTIC VERSUS NUMERIC X_h

Roberts et al. (2010) estimates X_h as (C1) as a function of expansion time-scale, entropy, and electron fraction

$$X_h \approx \begin{cases} 1 - \exp\left[-8 \times 10^5 Y_e^3 \left(\frac{\tau_{exp}}{ms}\right)\left(\frac{S}{k_B nuc^{-1}}\right)^{-3}\right], & Y_e < 0.5 \\ 1 - \left[1 + 140(1 - Y_e^2)\left(\frac{\tau_{exp}}{ms}\right)\left(\frac{S}{k_B nuc^{-1}}\right)^{-2}\right]^{-1/2}, & Y_e \geq 0.5. \end{cases} \quad \text{(C1)}$$

In Fig. C1, we show that the analytic expression predicts an X_h that is $\sim 50-90$ per cent higher than what is produced with `SkyNet` numerically. When nucleosynthesis is most conducive for this model, there is a ~ 50 per cent difference that increases significantly at later IC times and for greater Y_e. Numerically, it also is much more sensitive to the electron fraction for this range. In proton-rich conditions, we find it very difficult to synthesize large fractions of heavy elements. These differences do depend on the particular configuration of B_{dip} and P_0, however. Finally, as IC time increases, X_h decreases in the numerical implementation (and, in the limiting late-IC-time case, goes to zero). With the analytical expression, we see no time dependence in neutron-rich conditions and an inverse time dependence in proton-rich conditions.

These differences likely arise from a few key assumptions made in the analytic expression and may not apply well to the model studied in this work. First, Roberts et al. (2010) does not consider a magnetically dominated outflow; the rapid rotation from misaligned magnetars leads to an overall entropy decrease, although this decrease is only by a factor of ~ 2. This work also uses a limited 19-isotope nuclear network; a larger network with updated reactions may result in different results. Unlike in the numerical calculations of `SkyNet`, the analytical estimate assumes dominant reaction channels. For neutron-rich conditions, the reaction sequence is ^{4}He(αn, γ)^{9}Be(α, n)^{12}C and for proton-rich conditions, α particles recombine into ^{12}C via the triple-α reaction. The effective τ_{exp} and S dependence of X_h may not be described by the same polynomial as in the analytical treatment.

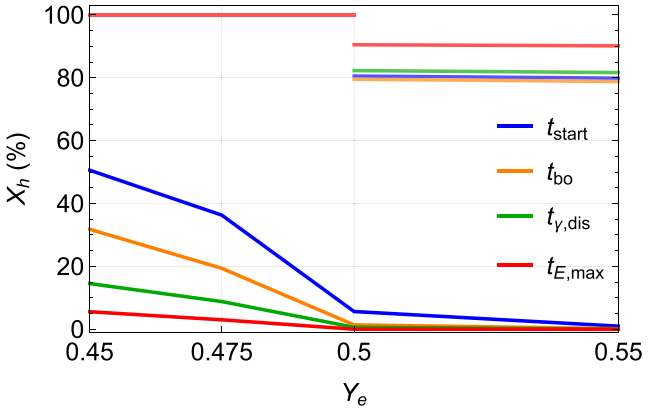

Figure C1. Comparison of analytic (equation 15) and numeric (this work) X_h for $B_{dip} = 5 \times 10^{15}$ G, $P_0 = 2$ ms model. Analytic is given by the translucent lines (all $\sim 80-100$ per cent) while numeric is given by opaque colors.

In the analytic expression, the only temporal variance arises in proton-rich conditions, since for $Y_e \lesssim 0.5$, $X_h \approx 1$ throughout. In that case, X_h rises with increasing time post-CC (with the ICs derived in this work). However, X_h numerically trends with ρ and T. These ICs depend on τ_{exp} and S, but to different order, and also are a function of mass-loss rate and include the dynamical evolution of NS radius. When including these, the ICs (and thus, heavy element nucleosynthesis) decrease with time. In the limiting case, heavy elements are not produced at all.

This paper has been typeset from a TEX/LATEX file prepared by the author.